Phonon dynamics in AlN lattice contaminated by oxygen

M. Kazan [a],*, B. Rufflé [b], Ch. Zgheib [a], P. Masri [a]

[a] Groupe d'Etude des Semiconducteurs, CNRS-UMR 5650, cc 074, Université Montpellier II, 34095, Montpellier, France
[b] Groupe Physique des Verres et Spectroscopies Laboratoire Colloïdes, Verre et Nanomatériaux Université Montpellier II, CC 069, 34095 Montpellier, France

Abstract

The phonon dynamics of wurtzite aluminum nitride contaminated by oxygen were investigated by employing the Raman back scattering, the Fourier Transform Infrared (FT-IR) reflectivity and absorption, and the Brillouin scattering techniques on unseeded polycrystalline samples of AlN built of single crystallites 1–5 mm in size. The six Raman active zone center optic modes were observed and identified. Throughout the oxygen contamination range (~1, ~2, and ~6 at.%) of three samples investigated, the widths of the principal Raman modes were found to decrease with increasing the oxygen content in the single crystal. This behavior is interpreted as a change in the nature of the oxygen defect when the oxygen concentration exceeds 1 at.%. The FT-IR reflectivity spectrum exhibits two-mode behavior at low oxygen concentration, one-mode behavior tends to be dominant when the oxygen concentration increases, and only one-mode behavior can be observed at high oxygen concentration. These changes in the reststrahlen band with oxygen concentration support the hypothesis of a transition in the oxygen accommodation defect as the concentration of oxygen increases. The oxygen effects on the AlN optical parameters were investigated by calculating these optical parameters from the reflectivity data of single crystallites differing in their oxygen concentration. The FT-IR absorption measurements showed several absorption bands in the multiple-phonon region. A tentative interpretation is proposed in which these bands are considered to be due to oxygen impurity absorption and to a combination of several phonon branches at the Brillouin-zone boundaries. The absorption spectrum in the one-phonon region allowed us to obtain a reliable data on the phonon density of states function in bulk AlN. Lastly, three different configurations were used in Brillouin scattering measurements to achieve a complete determination of the elastic stiffness constants of AlN.
© 2006 Elsevier B.V. All rights reserved.

1. Introduction

Aluminum nitride has attracted much attention because of its extreme values of fundamental physical and chemical properties which make it adequate for fabrication of a variety of devices capable of performing at extreme conditions of power, frequency, temperature, and in harsh environment [1]. Its wide band gap (6.2 eV at room temperature) [2] has led to investigations of its great potential for the development of optoelectronic devices operating near the short-wavelength end of the visible spectral range. AlN also has attractive piezoelectric properties which may be suitable for surface acoustic wave (SAW) device applications [3,4]. All these applications of AlN require detailed knowledge of the optical and acoustical modes of the single crystal.

Moreover, in the design of optoelectronic devices, interplay between the physical dimensions of the device and the optical parameters requires that each optical parameter be known as a function of the wavelength as precisely as possible.

A variety of experimental [5–10] and theoretical [11,12] techniques were used to probe the vibrational spectrum and optical parameters of AlN. However, there are significant discrepancies between the data reported. These disagreements come perhaps from the lack of suitable crystals for good measurements or probably because of several percent oxygen incorporation in the AlN lattice. Several models on the oxygen behavior in AlN are

* Corresponding author. Present address: CC 074, Groupe d'Etude des Semiconducteurs, Université Montpellier II, Place E. Bataillon, 34095 Montpellier Cedex 5 France. Tel.: +33 6 32 07 99 74, +33 4 67 14 32 97; fax: +33 4 67 14 37 60.
E-mail address: michel.kazan@ges.univ-montp2.fr (M. Kazan).

reported [13–15] in order to understand its effects on the AlN properties.

In this work, in order to give the reader the much possible experimental information about the phonon dynamics in the AlN lattice where several percent oxygen incorporation is possible, we have employed the Raman back scattering, the Brillouin scattering in three different configurations, and the FT-IR reflectivity and absorption techniques on three samples characterized by different oxygen contents (~1, ~2, and ~6 at.%). Our results are presented as a function of the oxygen content in the sample in order to illustrate the oxygen effects on the AlN properties.

2. Experiments

The crystal growth was accomplished by sublimation of an AlN charge placed in the hot zone of the tungsten crucible and subsequent condensation of vapor species in a cooler region. Prior to use for crystal growth, commercially available AlN powder was annealed in vacuum and subsequently resublimed in high-purity nitrogen at 2325 °C in order to reduce oxygen contamination of the AlN source material. The growth experiments were made in which the growth temperature on the crucible lid was set to 2225 °C. The furnace was operated in high-purity N_2 gas at pressure below 1000 mbar. A polycrystalline, dense boule of 2 in. in diameter and up to 10 mm in height was produced. Bulk samples were brown and partially non-transparent in particular because of grain boundaries decoration. The single crystallites which build these samples were strongly textured and were as big as 5×3 mm as it is shown in Fig. 1. The result of these growth experiments was three polycrystalline samples differing in their oxygen contamination. The variation of oxygen content in the samples comes from the variation of the purity of the source material.

High quality surfaces for Raman, FT-IR, and Brillouin measurements were prepared by chemical polishing performed in an identical way for all of the samples investigated to remove oxide films immediately prior to the measurements.

The orientation of each crystallite was evaluated from X-ray Laue back scattering using X'pert-MRD. The X'pert-MRD comprises a MRD Cradle having approximately $37 \times 44 \times 34$ cm ($W \times H \times D$) like dimensions and five motorized movements:

Fig. 1. A micrograph of polycrystalline bulk AlN material built of grains 1–5 mm in size.

Phi rotation (φ) (range $\geq 2 \times 360°$, step size: 0.02°); Psi tilt (ψ) (range: 180°, step size: 0.01°); X/Y manipulation (range: 100 mm, step size 0.01 mm). The measurements are therefore always taken at a fixed 2 Theta value and the single crystal orientation is realized by two movements: the Phi rotation axis, which is around the sample normal; the Psi rotation axis, which lies in the sample surface, and in the diffraction plane.

The Raman measurements in the back scattering geometry were performed at room temperature using 5145 Å light (in order to decrease the surface effect) from an Ar^+ laser of ~100 mW. A double monochromator was used to analyze the scattered radiation with a resolution of less than 1 cm^{-1}. The spot size on the crystallites was ~2 μm. The Raman measurements were taken on two crystal facets: a single crystal facet having the (0002) orientation, and a cut so that the c-axis or the optical axis was parallel to the single crystal facet (as it is judged by the X-ray measurements).

The FT-IR reflectivity and absorption measurements were performed at room temperature in the 400–3000 cm^{-1} frequency range using a KBr beamsplitter and a DTGS detector with a resolution of less than 1 cm^{-1} and an unpolarized light near normal incidence. The spectrometer used supplies an FT-IR microscope operating in reflectivity and absorption modes. This microscope was used only in the reflectivity measurements in order to measure the reflectivity from well definite facets, while the FT-IR absorption measurements were performed in vacuum to minimize the effect of atmospheric water-vapor absorption. The crystallites surface roughness was negligible compared with the wavelengths used in our FT-IR measurements, so that normalization of the spectra was not necessary.

The Brillouin measurements were performed at room temperature with incident $\lambda_0 = 5145$ Å monomode laser excitation of ~100 mW. A Sandercock [16] six-pass tandem Fabry-Perot interferometer (FPI) was used to analyze the light scattered from the crystallites. Brillouin spectra were recorded with a multichannel scale with 1024 channels and were accumulated ~5000 times with 1 ms/channel scan. The free spectra range of the FPI was set to 100 GHz and calibrated to better than 0.1 GHz with a reference sample (Li_2O-$2B_2O_3$ glass $\Delta v_{LA} = 42.06 \pm 0.01$ GHz in the back scattering geometry). The AlN crystallites investigated were partially non-transparent, so that it was not possible to use the platelet scattering geometry where the scattering vector is independent of the refractive index. The Brillouin spectra were taken on the two crystal facets used in the Raman measurements to achieve a complete determination of the elastic stiffness constants of AlN.

3. Results and discussion

3.1. Raman measurements

AlN has wurtzite structure with c_{6v}^4 symmetry. There are 4 atoms per unit cell leading to [17]: an A_1 branch in which the Raman-active phonon is polarized in the z direction and which is infrared active in the extraordinary ray; an E_1 branch in which the phonon polarized in the xy plane can be observed in the infrared in the ordinary ray spectrum, and which is also Raman
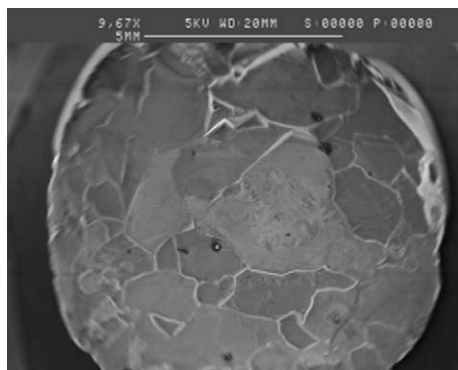
active; two E_2 branches which are Raman active; and two silent B_1 modes [18].

The nonvanishing components of the polarizability tensor are presented below for each mode, and for the polar phonons the direction of polarization is indicated in parenthesis.

$$A_1(z) = \begin{bmatrix} a & 0 & 0 \\ 0 & a & 0 \\ 0 & 0 & b \end{bmatrix}; \quad E_1(x) = \begin{bmatrix} 0 & 0 & c \\ 0 & 0 & 0 \\ c & 0 & 0 \end{bmatrix};$$
$$E_1(y) = \begin{bmatrix} 0 & 0 & 0 \\ 0 & 0 & c \\ 0 & c & 0 \end{bmatrix}; \quad E_2 = \begin{bmatrix} d & d & 0 \\ d & -d & 0 \\ 0 & 0 & 0 \end{bmatrix}. \quad (1)$$

The frequency of an optical phonon which is infrared active is split into a longitudinal (LO) and a transverse (TO) component by the macroscopic electric field associated with the longitudinal phonon. This electric field serves to stiffen the force constant of the phonon and thereby raise the frequency of the LO over that of the TO [19]. The consequences of this process on the static dielectric constant (ε_0) of the crystal are expected by the well-known Lyddane–Sachs–Teller relationship:

$$\varepsilon_0 = \varepsilon_\infty (w_{LO}/w_{TO})^2 \quad (2)$$

where w_{LO} and w_{TO} are the frequencies of the longitudinal and transverse components, respectively, and ε_∞ is the high-frequency dielectric constant.

Moreover, in the case of the wurtzite structure, the electrostatic forces dominate over the anisotropy in the short-range forces, the LO–TO splitting must be greater than the A_1–E_1 splitting. In other words, it should be a significant frequency separation between the group of the TO phonons relative to that of the LO phonons.

From what is discussed above, it may be readily determined which phonons must be seen in a variety of orientations where the phonon must conserve energy ($v = v_i - v_s$) and momentum ($q = k_i - k_s$).

In the notation we will follow in this paper a spectrum is described by four symbols, two inside a parenthesis and two outside. The symbols inside are, left to right, the polarization of the incident and scattered light, while the ones to the left and right of the parenthesis are the propagation directions of the incident and of the scattered light, respectively. Since in our measurements all of the Raman spectra were acquired in a back scattering geometry, the symbols outside the parenthesis will be the same.

In Fig. 2(a) for this $y(xx)y$ arrangement, since the incident light is propagating in the y direction and polarized along x, and the scattered light is also propagating along y and polarized along x, the predicted phonons are A_1(TO) at 610 cm^{-1} and E_2 (high frequency) at 656 cm^{-1}. Similarly, in Fig. 2(b), for the incident and scattered light are propagating along z direction and polarized along y the $z(yy)z$ arrangement gives E_2 (low frequency) phonon at 248 cm^{-1}, A_1(LO) phonon at 889 cm^{-1}, and the E_2 (high frequency) phonon already observed in the precedent arrangement. In Fig. 2(c), the incident light is propagating in the y direction and polarized along x, while the scattered light is polarized along z. This arrangement which is designed by $y(xz)y$, gives only one E_1(TO) phonon at 669 cm^{-1}. However, the $y(zy)x$ is the only arrangement which can give the
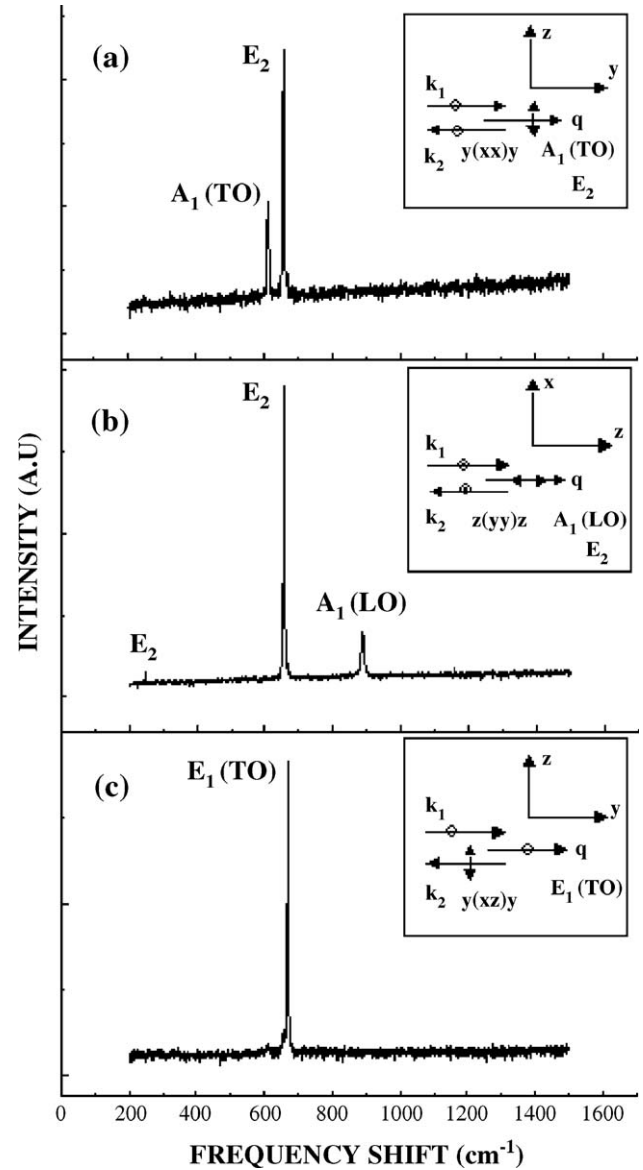

Fig. 2. Raman spectra of AlN. Inset: back scattering diagram for each orientation. The direction of the incident and scattered photons are indicated by k_i and k_s, respectively, and the optical phonon by q. The polarization directions are indicated by small arrows or by circled crosses, the latter indicating a direction perpendicular to the plane of the paper. The predicted phonons are listed below each diagram.

E_1(LO) phonon. This arrangement was not possible due to the partial non-transparency of our samples (see Section 2). But this phonon mode can be probed by the FT-IR reflectivity measurements as it will be shown later.

After identifying the symmetry of each of the Raman active phonons it will be interesting to discuss the lifetimes of these phonons which can be deduced from the Raman measurements. One fundamental mechanism that affects phonon lifetimes in semiconductors is the anharmonic decay of a phonon into other Brillouin zone phonons such that the energy and momentum are conserved in the process. However, other additional channels of phonon decay are clearly possible especially in material containing impurities and defects. Theses crystal imperfections can destroy the translational symmetry of the crystal, and thus,

perturb the characteristic lifetime of the propagating phonon. The Raman line width ΔE can be used to evaluate the phonon lifetime τ via the energy-time uncertainty relation:

$$\Delta E/\hbar = 1/\tau. \qquad (3)$$

Therefore, one may expect an increase in the Raman line width with increasing the concentration of the oxygen impurities in AlN. However, our findings indicate that the line width of the Raman modes decrease with increasing the oxygen concentration. This oxygen effect on Raman line width is already observed by McNeil et al. [10] when the oxygen content in the sample exceeds ~1 at.% and is interpreted as a change in the oxygen accommodation defect as the concentration of oxygen increases. It will be shown later that this behavior can be observed also from the line widths of the loss energy functions (which denotes the longitudinal mode) deduced from the re-

flectivity data of several AlN crystallites differing in their oxygen concentration.

3.2. FT-IR reflectivity measurements

As it is well seen in Fig. 3, significant changes can be observed in the FT-IR reflectivity spectrum when the oxygen concentration increases in the sample. Throughout the oxygen contamination range (~1, ~2, and ~6 at.%) of three crystallites measured, the FT-IR reflectivity spectrum shows two reststrahlen bands, (i) a strong band which is shifted down in frequency monotonically as the oxygen concentration increases, and (ii) a higher frequency weak band which appears only at low oxygen concentration (~1 at.%) which weakens when the oxygen concentration increases (~2 at.%) and vanishes completely at high oxygen concentration (~6 at.%). This vanishing of the high frequency weak band is accompanied by
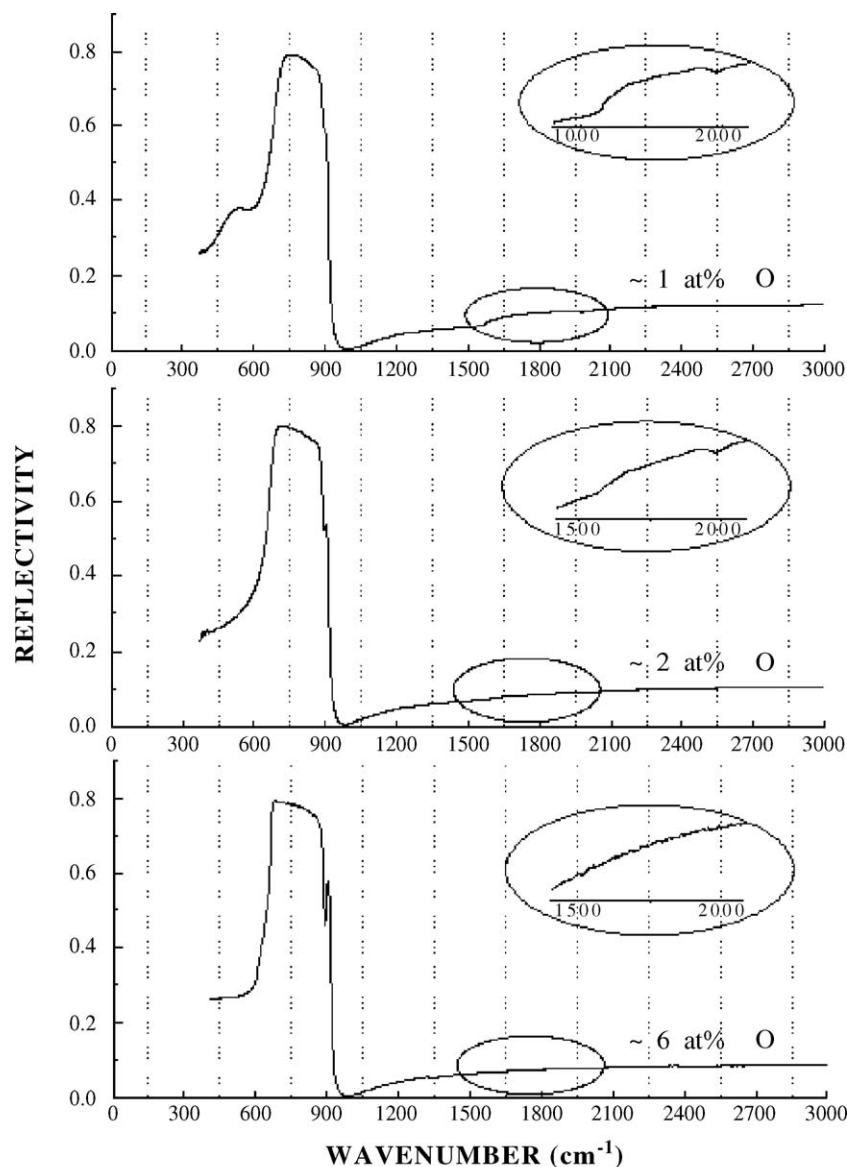

Fig. 3. Reflectivity spectra of the three AlN crystallites investigated. Inset: the behavior of an additional reststrahlen band throughout the oxygen contamination range of the three crystallites investigated. A vertically grid figures are used to show the downwards shift of the main reststrahlen band.

the appearance of a weak structure near 890 cm^{-1} which increases in magnitude with increasing oxygen concentration. A deformation at the lower edge of the main reststrahlen band occurs at low oxygen concentration only.

One can distinguish two type of infrared reflectivity behavior in binary semiconductors containing a high concentration of impurity such as AlN (which seems to present an extreme case in this respect, because of the possibility of several percent oxygen incorporation [13]): two-mode behavior which is characterized by the occurrence of two distinct reststrahlen bands and one-mode behavior in which the reststrahlen band of the host crystal and the local vibration mode merge into a single reststrahlen band. The changes in the reststrahlen band as well as the occurrence of one or two mode behavior are well understood on the basis of local mode theory. The criteria for two-band behavior are that, in the heavier ion compound, the local mode due to the substituted ion must fall above the optical branch of the host crystal spectrum and that, similarly, in the lighter ion compound, the substituted impurity must give rise either to a localized gap mode between the acoustical and optical branches of the parent crystal, or to an in-band resonance mode. One criterion for localized gap mode and consequently two-mode behavior is that the phonon dispersion of the host crystal be such a gap does exist between its acoustical and optical branches. AlN in its wurtzite structure does not have such a gap [21,22], and it therefore follows that any impurity, that substitutes for nitrogen, with an atomic mass larger than that of nitrogen cannot exhibit the conventional two-mode behavior. Therefore, strict one-mode behavior is possible when an impurity with a larger mass than that of nitrogen substitutes for nitrogen. This implies that two distinct reststrahlen bands in the reflectivity spectrum of AlN can appear only if an oxygen impurity substitutes for aluminum atom (which is the heavier atom).

From what is discussed above, we can attribute the deformation occurring at the lower edge of the main reststrahlen band observed in the reflectivity spectrum of the purest sample to an in-band resonance mode within the 248–400 cm^{-1} (E_2 optical mode frequency) range frequency caused by nitrogen vacancies substituted by oxygen atoms. Observation of the reflectivity spectra in this frequency range was not possible because it was out of the limit of our detector. The two-mode behavior and consequently the high-frequency weak reststrahlen band which appears in the reflectivity spectrum of the purest sample is attributed to an Al vacancy substituted by oxygen (which has a smaller atomic mass). The vanishing of the two-mode behavior as well as the appearance of the sharp structure near 890 cm^{-1} when the oxygen concentration increases strongly suggest that a transition in the oxygen defect accommodation occurs when the concentration of oxygen increases. These observations support the hypothesis (deduced earlier from the behavior of the Raman line width) of a change in the nature of the oxygen defect as the oxygen concentration increases.

3.3. Derivation of the optical parameters

The coefficient $r(\omega)$ is a complex function which is defined at the surface of the crystal as being the ratio between the reflective and the incident electric field:

$$r(\omega) = \frac{E_r}{E_i} = \rho(\omega)e^{i\theta(\omega)}, \tag{4}$$

where the amplitude $\rho(\omega)$ and the phase shift of the reflected electric field $\theta(\omega)$ were separated.

The phase shift can be given by:

$$\theta(\omega) = \frac{2\omega}{\pi} \int_0^{\infty} \frac{\ln r(\omega') - \ln r(\omega)}{\omega^2 - \omega'^2} d\omega'. \tag{5}$$

The reflectivity index n and the extinction coefficient k of a crystallite are related to its reflectivity at normal incidence by the relation:

$$r(\omega) = \frac{n + ik - 1}{n + ik + 1} = \frac{\sqrt{\varepsilon} - 1}{\sqrt{\varepsilon} + 1}, \tag{6}$$

where ε is the complex dielectric constant.

The quantity which is measured in experiments is the reflectivity $R(\omega)$. It is given by the relation:

$$R(\omega) = r(\omega)r^*(\omega) = \rho^2. \tag{7}$$

We can see from Eqs. (4) (5) (6) and (7) that the optical parameters n and k or alternatively the real and the imaginary parts of the dielectric constant ε_1 and ε_2 can be known as a function of frequency from the reflectivity measurements only. Since the oxygen affects deeply the AlN reflectivity spectrum as it is shown earlier, significant oxygen effects on the AlN optical parameters may be expected. In order to probe these effects, each optical parameter was calculated from each reflectivity spectrum illustrated in Fig. 3 and the results are plotted together in Fig. 4.

The optical transverse frequency w_{TO} is located at the maximum of ε_2, and the optical longitudinal frequency w_{LO} occurs at the maximum of the loss energy function Im$(-1/\varepsilon)$. Since the FT-IR reflectivity measurements were performed at near normal incidence using unpolarized light on crystallites oriented along the c-axis, the maxima of ε_2 and Im$(-1/\varepsilon)$ can be attributed, respectively, to the E_1(TO) and the E_1(LO) phonon frequencies.

It is well seen from Fig. 4 that the line widths of the ε_2 and Im$(-1/\varepsilon)$ peaks decrease with increasing the oxygen concentration. This behavior is in good agreement with what it was observed in the Raman measurements when the line widths of the Raman peaks decrease with increasing the oxygen concentration.

Otherwise, with increasing oxygen concentration, the E_1(TO) and E_1(LO) frequencies shift downwards and a weak maximum attributed to in-band resonance mode observed in the plot of Im$(-1/\varepsilon)$ increases in magnitude. This behavior also support the hypothesis of a transition in the oxygen accommodation defect as the oxygen concentration increases.

The three spectra of ε_1 were extrapolated to zero and three values of static dielectric constant ε_0 were obtained: 8.22 for the crystallite containing ~6 at.% of oxygen, 7.92 for the crystallite containing ~2 at.% of oxygen, and 7.87 for the crystallite containing ~1 at.% of oxygen. Therefore, the high-frequency dielectric constant ε_∞ can be calculated as a function of the
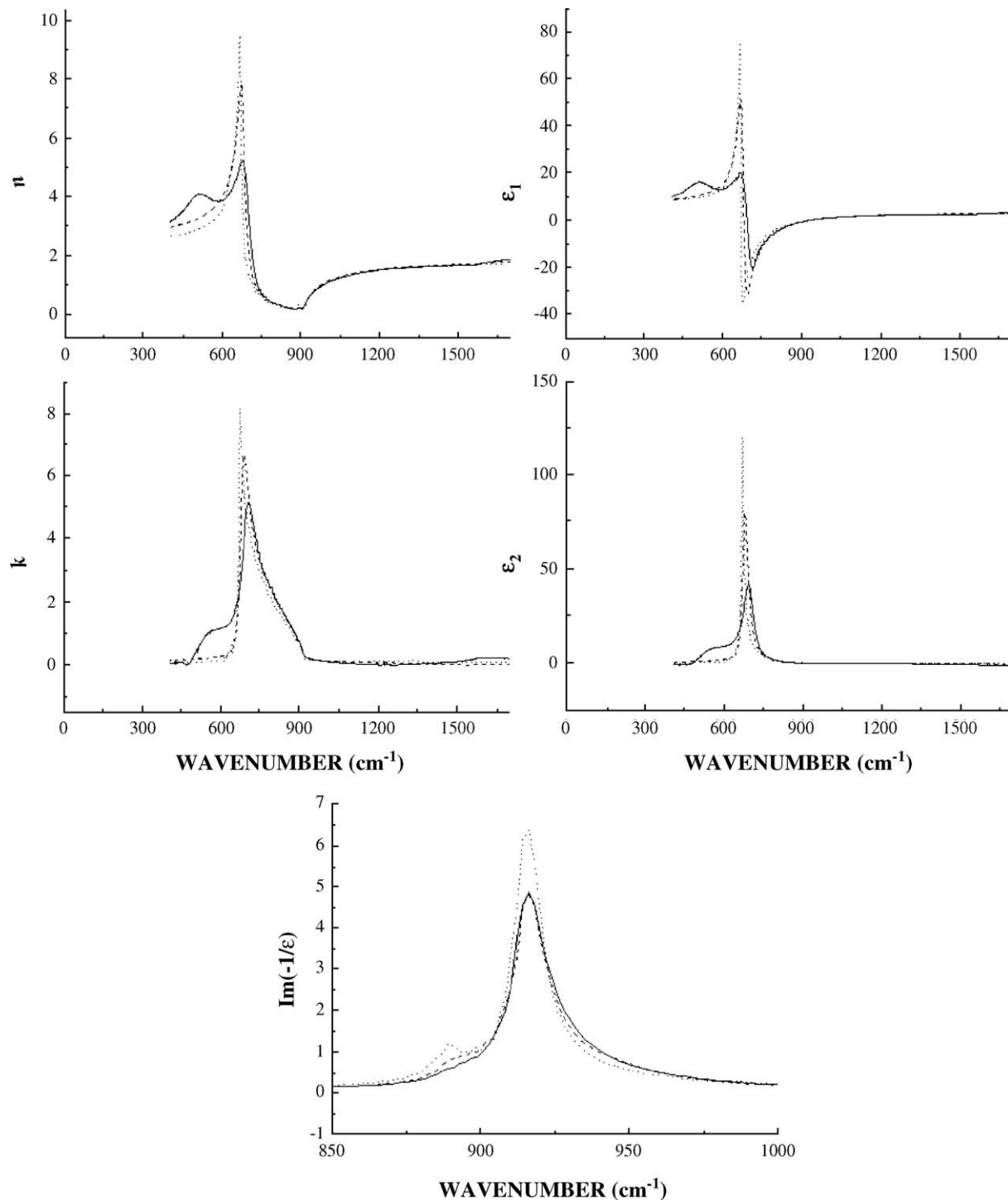
Fig. 4. Optical parameters of AlN calculated from the reflectivity spectra. Solid line: plot of the optical parameters calculated from the reflectivity spectrum of the crystallite containing ∼1 at.% of oxygen. Dashed line: plot of the optical parameters calculated from the reflectivity spectrum of the crystallite containing ∼2 at.% of oxygen. Dotted line: plot of the optical parameters calculated from the reflectivity spectrum of the crystallite containing ∼6 at.% of oxygen.

oxygen concentration by using Eq. (2). By substituting the correspondent values of w_{TO}, w_{LO}, and ε_0, three values of ε_∞ were obtained: 4.38 for the crystallite containing ∼6 at.% of oxygen, 4.39 for the crystallite containing ∼2 at.% of oxygen, and 4.51 for the crystallite containing ∼1 at.% of oxygen.

If we assume now that the high-frequency dielectric constant is the square of the refractive index in the visible n_∞, we obtain

three close values of n_∞: 2.0928 for the crystallite containing ∼6 at.% of oxygen, 2.0952 for the crystallite containing ∼2 at.% of oxygen, and 2.1237 for the crystallite containing ∼1 at.% of oxygen.

Since we have derived these values from reflectivity measurements at normal incidence on crystallites oriented along the c-axis, all these values will refer to as the ordinary

values. The extraordinary values can be obtained by using the value of the anisotropy of AlN calculated in Ref. [12] where the anisotropy of the static and high-frequency dielectric constant was found to be: $\varepsilon_0\,(//)/\varepsilon_0\,(\perp)=\varepsilon_\infty\,(//)/\varepsilon_\infty\,(\perp)=1.04$.

3.4. FT-IR absorption measurements

All these results presented above provide information about the phonon dynamics at the Brillouin zone center and about the effect of oxygen impurity on the lattice vibration and the optical parameters of AlN. However, FT-IR absorption measurements can provide additional information on the vibrational spectrum of the crystal lattice at the Brillouin zone edge. In Fig. 5 we present the FT-IR spectra of thin (∼100 μm) substrate of AlN.

In the two- and three-phonon region the finite size effect can be neglected in our measurements due to the large enough crystallites which built the sample used in these measurements (see Section 2). Therefore, the strong intrinsic absorption bands which are observed in the FT-IR absorption spectrum in the multiple-phonon region are generally considered originate from impurities absorption or multiple-phonon combinations involving of an infrared photon with two or three lattice phonons and are due to singularities in the phonon frequency distribution. These singularities arise from critical points in the Brillouin zone where $(\partial/\partial K)\,(\omega_1+\omega_2)=0$ (if we consider a two-phonon combination) where K is the wave vector and ω_1 and ω_2 are the frequencies of the combined phonons. This condition often occurs at $K=K_{\max}$ where $(\partial\omega_1/\partial K)$ and $(\partial\omega_2/\partial K)$ are separately equal to zero. However, there are several factors that make the assignments of the absorption bands in the multiple-phonon region to the phonons of definite types and symmetry very difficult. First, we expect that the oxygen affects the lattice vibration spectrum at the Brillouin zone edge in the same manner that it affects the lattice vibration spectrum at the Brillouin zone center, and it follows that the prediction of the phonon frequencies at the Brillouin zone edge will be rarely possible. Se-
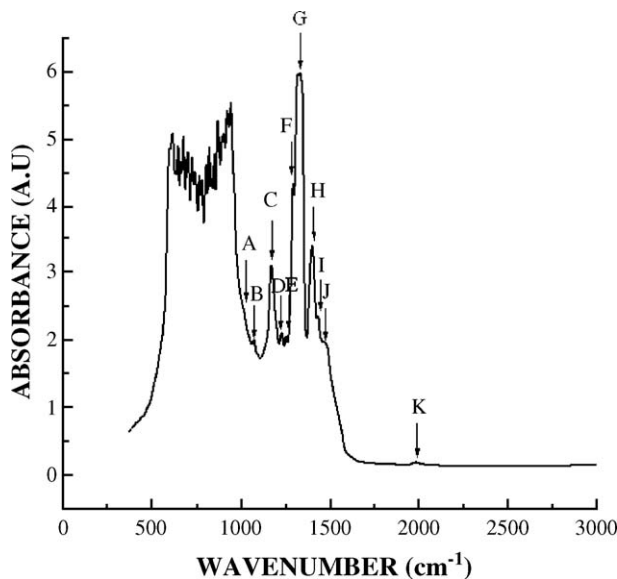
Table 1
Assignment of absorption bands observed in FT-IR absorption to impurity absorptions and multiple-phonon combinations

Frequency (cm^{-1})	Assignment	Point
A) 1020	$A_1(TO)+TA_1$	K
B) 1073	$E_1(TO)+LA$	M
C) 1172	$E_1(LO)+LA$	K
D) 1231	$3LA$	M
E) 1256	$2A_1(TO)$	M
F) 1295	$E_1(TO)+A_1(TO)$	M
G) 1332	$2E_1(TO)$	M
H) 1403	$E_1(LO)+A_1(TO)$	K
I) 1435	$2TA_2+A_1(TO)+TA_1$	M
J) 1475	$2E_1(LO)$	K
K) 1984	Oxygen impurity	

The frequencies used are estimated from [20] and [21]. The longitudinal acoustic branch is referred to as LA and the two transverse branches are referred to as TA$_1$ and TA$_2$.

cond, critical points may occur well inside the Brillouin zone if the condition that $(\partial/\partial K)\,(\omega_1+\omega_2)=0$ is satisfied over a sufficiently large interval ΔK [22]. In other words, The combination bands associated with the zone boundary phonons may be associated with a single critical point.

We have tabulated in Table 1 a tentative interpretation of the absorption bands appearing in the multiple-phonon region in which we involved fundamental frequencies of the Brillouin zone edges taken from the literature [20,21]. All the bands appearing in the FT-IR absorption spectrum were attributed to multiple-phonon combination at the Brillouin zone boundaries except the band at 1984 cm^{-1} which is probably due to oxygen impurity substituting an Al atom (see the additional weak band at this frequency appearing in the reflectivity spectrum).

Although the E_2 and B_1 branches are not infrared-active, the FT-IR absorption in the one-phonon region seems to be a useful method for probing the phonon density of states (DOS) function. A comparison of the FT-IR absorption spectrum in the one-phonon region with previously reported experimental data obtained in low-temperature neutron studies of AlN powder [23] or in room- and low-temperature measurements of second-order Raman scattering from strongly disordered AlN samples [24] shows that FT-IR absorption can provide means to obtain a reliable data on the phonon density of states.

3.5. Brillouin measurements

We have discussed above the optical phonon dynamics in wurtzite AlN. Although the knowledge of the optical modes in AlN are strongly required for some applications in electroluminescent devices, other applications such as the manufacturing of surface acoustic waves (SAW) devices require knowledge of the acoustical vibrational modes and of the bulk elastic constants of the material. Brillouin scattering can provide a determination of these modes and elastic constants.

As AlN has an hexagonal structure with a space group c_{6v}^4, five independent elastic constants have to be determined.

The single crystal used for this Brillouin scattering experiments was brown in color (see Section 2), so that it was not possible to use the platelet scattering geometry where Q the
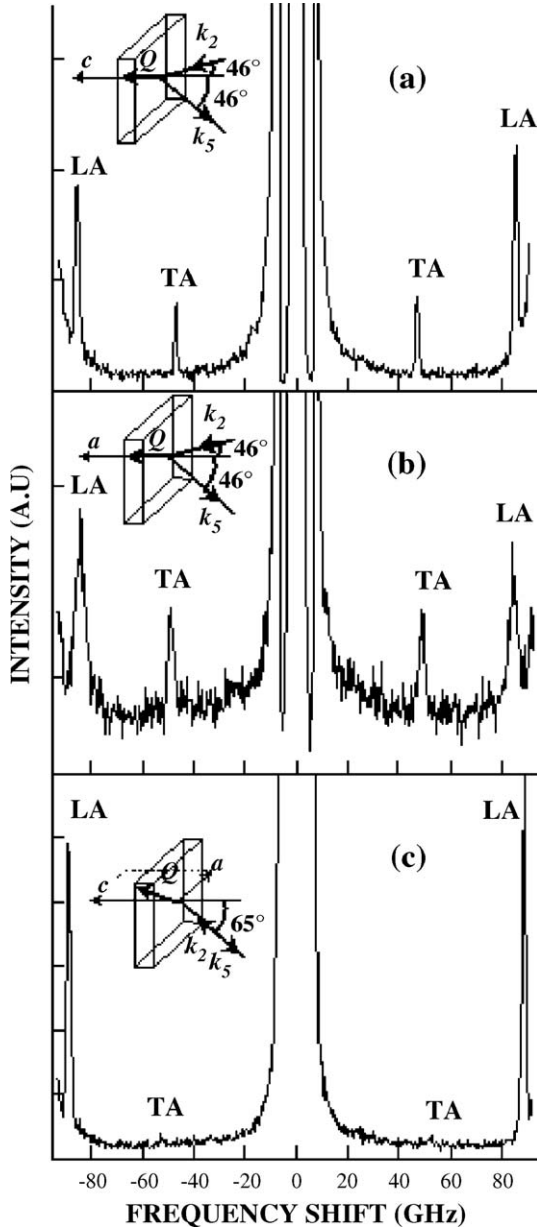

Fig. 5. Absorption bands in the multiple-phonon region.

Fig. 6. Brillouin spectra of AlN. Inset: experimental arrangements with $V - V + H$ polarization. The direction of the incident and scattered photons are indicated by k_i and k_s, respectively, and the acoustic phonon by Q. (a) phonon propagating along the c-axis. (b) phonon propagating perpendicular to the c-axis. (c) phonon propagating in the ac-plane at an angle of 24.9° with the c-axis.

C_{33} and C_{44} modes, respectively. The phonon velocity V is related to the Brillouin shift frequency Δv by:

$$V = \lambda_0 \Delta v [n^2 + n'^2 - 2nn' \cos\theta_{in}]^{-1/2}, \qquad (8)$$

Where n and n' are the appropriate refractive indices for incident and scattered photons, respectively, λ_0 is the vacuum wavelength of the radiation, and θ_{in} the scattering angle in the

Table 2
Summary of our results as a function of the oxygen concentration compared with previously reported results

	Oxygen concentration			Previously reported values	
	~1 at.%	~2 at.%	~6 at.%	Values	References
ω_T [a] (cm^{-1})	693.6	682.0	668.8	666.7	[8]
ω_L [b] (cm^{-1})	916.3	916.2	915.9	916.3	[8]
$\varepsilon_0(\perp)$	7.87	7.92	8.22	7.91, 7.82	[12]
$\varepsilon_0(//)$	8.12	8.24	8.55	8.22	[12]
				8.5	[28] [c]
				8.5	[29] [c]
$\varepsilon_\infty(\perp)$	4.51	4.39	4.38	4.53, 4.40	[12]
				1.23	[11]
$\varepsilon_\infty(//)$	4.69	4.57	4.55	4.72, 4.64	[12]
				4.68, 4.84	[28] [c]
				4.68	[30] [c]
				4.84	[8] [c]
$n_\infty(o)$	2.1237	2.0952	2.0928		
$n_\infty(e)$	2.1657	2.1367	2.1342	2.15	[5] [d]
				2.2	[31] [d]
E_2 (cm^{-1})			248	252	[10]
				303	[32]
$A_1(TO)$ (cm^{-1})			610	614	[10]
				613	[33]
E_2 (cm^{-1})			656	660	[10]
				658.7	[33]
$E_1(TO)$ (cm^{-1})			669	673	[10]
				671.7	[33]
$A_1(LO)$ (cm^{-1})			889	893	[10]
				892.7	[33]
C_{11} (GPa)			394.1 ± 1	410 ± 10	[10] [e]
				345	[27] [e]
				398	[26] [f]
C_{33} (GPa)			402 ± 1	388.5 ± 10	[10] [e]
				395	[27] [e]
				382	[26] [f]
C_{44} (GPa)			120.1 ± 1	124.6 ± 4.5	[10] [e]
				118	[27] [e]
				96	[26] [f]
C_{12} (GPa)			133.4 ± 2	148.5 ± 10	[10] [e]
				125	[27] [e]
				140	[26] [f]
C_{13} (GPa)			95.2 ± 1	98.9 ± 3.5	[10] [e]
				120	[27] [e]
				126	[26] [f]

[a] The transverse optical mode frequency calculated from the reflectivity measurement.
[b] The longitudinal optical mode frequency calculated from the reflectivity measurement.
[c] Average values of transverse and longitudinal directions.
[d] Average values of the ordinary and extraordinary refraction indexes.
[e] Experimental measurements.
[f] ab initio calculation.

scattering vector is independent of the refractive index n. Three different configurations were used to achieve a complete determination of the elastic stiffness constants of AlN. In the first configuration, spectra were taken in the right angle scattering geometry ($\theta_{ext} = 92°$) where the wave vector Q of the acoustic phonon is parallel to the c-axis. The polarizations of incident and scattered lights were V and $V + H$, respectively. In this direction of high symmetry, the solution to the Christoffel equation for ρV^2 are two pure modes: the C_{33} longitudinal acoustic mode and doubly degenerate C_{44} shear acoustic mode. As it is shown in Fig. 6(a), the measured spectrum exhibits a polarized peak at 85.25 GHz and a depolarized peak at 46.97 GHz which can be assigned to the

crystal. The ordinary and extraordinary refractive indices were taken to correspond, respectively, to the values 2.0928 and 2.1342 (see in Section 3.3 the optical parameters of the crystallite containing ~6 at.% of oxygen). The elastic constants were obtained by using the density $\rho = 3.23$ g/cm^3 [25]. Next, Brillouin measurements were performed again with the same right angle geometry but this time the direction of the Q vector perpendicular to the c-axis. Three pure modes are expected: the C_{11} longitudinal acoustic mode, the $C_{66} = (C_{11} - C_{12})/2$ shear acoustic mode and the C_{44} shear acoustic mode. Forbidden by the selection rules for this scattering geometry, the latter cannot be observed. The Brillouin spectrum plotted in Fig. 6(b) presents a polarized peak at 84.38 GHz and a depolarized peak at 48.80 GHz related to the C_{11} and C_{66} mode, respectively. To obtain the last elastic constant C_{13} accurately, Brillouin measurements were performed in the back scattering geometry ($\theta_{ext} = 180°$) where the laser was directed onto the sample at an incident angle of $\alpha_{ext} = 45°$, $55°$, and $65°$ from the c-axis. In Fig. 6(c), where $\alpha_{ext} = 65°$, two mixed modes are observed. These two mixed modes are the quasi-longitudinal and the quasi-transverse acoustic modes, which are both expressed as a function of C_{13}, C_{11}, and C_{33}. From a fit of the experimental elastic stiffness constant in the ac-plane we deduced the value of the last constant C_{13}.

The values of the AlN elastic constants reported in this work are slightly different from those reported in [10] by McNeil et al. possibly due to a small differences in the AlN material quality or to that in our measurements we have used an ordinary and extraordinary refractive indexes values deduced from the FT-IR reflectivity spectra of the same crystallites used in the Brillouin measurements, while in those of McNeil et al. the used values of the reflective indexes of the medium (when the Brillouin measurements were performed in the back scattering geometry) seem to be taken from the literature.

We summarize our results on AlN vibrational properties in Table 2. These results are presented as a function of oxygen concentration in AlN. It is well seen that the oxygen concentration affects significantly the properties of AlN. We believe that the oxygen point defects in the samples can be a sufficient reason for that the measured properties of AlN tend to disagree with one another.

4. Conclusion

In this work we have measured the frequency and identified the symmetry of each of the Raman active zone center optic modes. Significant changes observed in the reflectivity spectra of several crystallites differing in their oxygen concentration have been interpreted as a transition in the oxygen defect accommodation as the concentration of oxygen increases. The optical parameters, deduced from the reflectivity spectra by using the Kramers-Kronig technique and the dispersion theory, have been found to be deeply affected by the oxygen concentration. The absorption bands observed in the FT-IR absorption spectrum on the high frequency range of the reflectivity band have been interpreted as a combination of several phonon branches at the Brillouin zone boundaries or as an oxygen impurity absorption. It has been found that the AlN DOS function can be estimated from the FT-IR absorption spectrum in the one-phonon region. We have made also a careful analysis of the Brillouin spectra to measure the five elastic constants of AlN. Our results are presented lastly as a function of oxygen concentration.

Acknowledgement

References

[1] A. Ishida, Y. Inowe, H. Nagasawa, N. Sone, K. Ishino, J.J. Kim, H. Makino, T. Yao, H. Kan, H. Fujiyasu, Physica, E, Low-Dimens. Syst. Nanostruct. 21 (2004) 540.
[2] W.M. Yim, E.J. Stofko, P.J. Zanzucchi, J.I. Pankove, M. Ettenberg, S.L. Gilbert, J. Appl. Phys. 44 (1973) 292.
[3] G.R. Kline, K.M. Larkin, Appl. Phys. Lett. 43 (1983) 750.
[4] K. Tsubouchi, K. Sugai, N. Mikoshiba, Jpn. J. Appl. Phys. 19 (1980) L751.
[5] G.A. Cox, D.O. Cummins, K. Kawabe, R.H. Tredgold, J. Phys. Chem. Solids 28 (1967) 543.
[6] J. Banes, L. Biste, D. Bloze, Phys. Status, Solidi, A Appl. Res. 39 (1977) 173.
[7] J.J. Hantzpergue, Y. Pauleau, J.C. Remy, D. Roptin, M. Callier, Thin Solid Films 75 (1981) 167.
[8] A.T. Collins, E.C. Lightowlers, P.J. Dean, Phys. Rev. 158 (1967) 833.
[9] Y. Fujii, S. Yoshida, S. Misawa, S. Maekawa, T. Sakudo, Appl. Phys. Lett. 31 (1977) 815.
[10] L.E. McNeil, M. Grimsditch, R.H. French, J. Am. Ceram. Soc. 76 (1993) 1132.
[11] Aleksandra B. Bjurisic, E. Herbert Li, J. Appl. Phys. 85 (1999) 2848.
[12] C. Persson, R. Ahyja, A. Ferreira da Silva, B. Johansson, J. Cryst. Growth 231 (2001) 407.
[13] R.A. Youngman, J.H. Harris, J. Am. Ceram. Soc. 73 (1990) 3238.
[14] Quanli Hu, Tetsuji Noda, Hisoshi Tanigawa, Toshiaki Yoncoka, Satoru Tanaka, Nucl. Instrum. Methods Phys. Res., B Beam Interact. Mater. Atoms 191 (2002) 536.
[15] T. Mattila, R.M. Nieminen, Phys. Rev., B 54 (1996) 16676.
[16] M. Cardona, in: M. Cardona, G. Güntherodt (Eds.), Light Sattering in Solids II, Topics in Applied Physics, vol. 50, springer, Berlin, 1982, p. 19.
[17] R. Loudon, Adv. Phys. 13 (1964) 423.
[18] M. Tinkham, Group Theory and Quantum Mechanics, McGraw-Hill, New York, 1964.
[19] Leah Bergman, Mitra Dutta, Cengiz Balkas, Robert F. Davis, James A. Christman, Dimitri Alexson, Robert J. Nemanich, J. Appl. Phys. 85 (1999) 3535.
[20] H.M. Tütücü, G.P. Srivastava, Phys. Rev., B 62 (2000) 5028.
[21] Claudia Bungaro, Krzusztof Rapcewicz, J. Bemhole, Phys. Rev., B 61 (2000) 6720.
[22] A.M. Karo, J.R. Hardy, I. Morrison, J. Phys. Radium 26 (1965) 668.
[23] C. -K. Loong, in: R.D. Dupuis, J.A. Edmond, F.A. Ponce, S. Nakamura (Eds.), Gallium Nitride and Related Materials, MRS Symposia Proceedings, vol. 395, Materials Research Society, Pittsburgh, 1995, p. 423.
[24] V. Yu. Davydov, Yu. E. Kitaev, I.N. Goncharuk, A.N. Smirnov, J. Graul, O. Semchinova, D. Uffmann, M.B. Smirnov, A.P. Mirogorodsky, Phys. Rev., B 58 (1998) 12899.
[25] Y. GoldBerg, in: Levinstein, Rumyantsev, Shur (Eds.), Properties of Advanced Semiconductor Materials, 2001, p. 31.
[26] Kwiseon Kim, Walter R.L. Lambrecht, Benjamin Segall, Phys. Rev., B 53 (1996) 16310.
[27] K. Tsubouchi, K. Sugai, N. Mikoshiba, in: B.R. McAvoy (Ed.), AlN Material Constants Evaluation and Saw Properties on AlN/Al$_2$O$_3$ and

AlN/Si, Ultrasonics Symposium Proceedings, IEEE, 1981, p. 375, (Chicago, IL, Oct.).

[28] S. Strite, H. Morkoç, J. Vac. Sci. Technol., B 10 (1992) 1237.

[29] J. Ducheme, Thin Solid Films 8 (1971) 69.

[30] I. Akasaki, H. Hashimoto, Solid State Commun. 5 (1967) 851.

[31] J. Patrnak, L. Roskkovcova, Phys. Status Solidi 14 (1966) K5.

[32] C. Carlone, K.M. Lakin, H.R. Shanks, J. Appl. Phys. 55 (1984) 4010.

[33] Jonathan M. Hayes, Martin Kuball, Ying Shi, James H. Edgar, Jpn. J. Appl. Phys. 39 (2000) L710.